Charge transport and exciton dissociation in organic solar cells consisting of dipolar donors mixed with C_{70}

Olga L. Griffith, Xiao Liu, Jojo A. Amonoo, Peter I. Djurovich, Mark E. Thompson, Peter F. Green, and Stephen R. Forrest

Phys. Rev. B **92**, 085404 — Published 6 August 2015

DOI: 10.1103/PhysRevB.92.085404

Charge Transport and Exciton Dissociation in Organic Solar Cells Consisting of Dipolar Donors Mixed with C_{70}

Olga L. Griffith,[1] Xiao Liu,[1] Jojo A. Amonoo,[2] Peter I. Djurovich,[4] Mark E. Thompson,[4] Peter F. Green,[2] and Stephen R. Forrest[1,3]

[1]Department of Electrical Engineering and Computer Science, University of Michigan, Ann Arbor, MI;

[2]Department of Material Science and Engineering, University of Michigan, Ann Arbor, MI;

[3]Department of Physics, University of Michigan, Ann Arbor, MI;

[4]Department of Chemistry, University of Southern California, Los Angeles, CA

ABSTRACT

We investigate dipolar donor materials mixed with a C_{70} acceptor in an organic photovoltaic (OPV) cell. Dipolar donors that have donor-acceptor-acceptor (d-a-a') structure result in high conductivity pathways due to close coupling between neighboring molecules in the mixed films. We analyze the charge transfer properties of the dipolar donor:C_{70} mixtures and corresponding neat donors using a combination of time-resolved electroluminescence from intermolecular polaron pair states and conductive tip atomic force microscopy, from which we infer that dimers of the d-a-a' donors tend to form a continuous network of nanocrystalline clusters within the blends. Additional insights are provided by quantum mechanical calculations of hole transfer coupling and hopping rates between donor molecules using nearest neighbor donor packing motifs taken from crystal structural data. The approximation using only nearest neighbor interactions leads to good agreement between donor hole hopping rates and the conductive properties of the donor:C_{70} blends. This represents a significant simplification from requiring details of the nano- and mesoscale morphologies of thin films to estimate their electronic

characteristics. Using these dipolar donors, we obtain a maximum power conversion efficiency of 9.6 ± 0.5 % under 1 sun, AM1.5G simulated illumination for an OPV comprised of an active layer containing a dipolar donor mixed with C_{70}.

I. INTRODUCTION

Paths to improving energy generation in organic photovoltaic (OPV) cells include blending donor (D) and acceptor (A) molecules in the active region to promote efficient exciton dissociation,[1-3] incorporating exciton blocking layers adjacent to the anode and/or cathode to prevent exciton quenching at the electrodes,[4-9] and using donor[10, 11] or acceptor[12] energy cascades to drive exciton transfer toward a dissociating interface. These strategies are designed to increase exciton harvesting by reducing exciton recombination while also increasing charge conduction away from the D-A heterojunctions. Recently, a class of molecules with large ground-state dipole moments have been introduced as a route to achieving high efficiency photon-to-charge conversion in D-A heterojunction OPVs.[13] Within these molecules are electron donating (d) and two different accepting (a, a') functional groups following the structure of d-a-a'. (Here lower case letters denote groups within a molecule while upper case D, A signify the donating or accepting nature of the entire molecule based on its frontier orbital energies relative to a second molecular species). In this work we study OPVs based on two such dipolar molecules that exhibit high conductivity when used in fullerene blends.

Large molecular dipole moments have been shown to lead to the energetic disorder in the film thus reducing the charge hopping rate.[14, 15] Here we show that the presence of large molecular dipole moments can be beneficial rather than disadvantageous for promoting charge hopping. Electrostatic attraction between the large fixed internal dipoles in these molecules leads to formation of centrosymmetric dimers with cofacial π-π antiparallel alignment along the long molecular axis.[13, 16-18] The net result is that the total dipole moment is zero for these cofacial π-π dimers. The dimers of the d-a-a' molecules 2-[(7-(4-[N,N-bis(4-methylphenyl)amino]phenyl)-

2,1,3-benzothia-diazol-4-yl)methylene] propane-dinitrile (i.e. DTDCPB[13], referred to here as CPB for simplicity), and 2-((7-(5-(dip-tolylamino)thiophen-2-yl)benzo[c][1,2,5]thiadiazol-4-yl)methylene) malononitrile (DTDCTB[13], CTB for simplicity; see **Scheme 1** for all molecular structural formulae) also display additional supramolecular ordering in the solid state with secondary end-to-side orientations. The resulting hole transfer coupling integrals (H_{ab}), as determined by direct coupling calculations for initial and final states prepared using constrained density functional theory (CDFT)[19] on neat CPB, CTB, and the non-polar 'control' tetraphenyldibenzoperiflanthene (DBP) films, are comparable to or even stronger than the π-orbital overlap in cofacial orientations. Modeling in combination with time-resolved electroluminescence suggest that the enhanced hole hopping from these unique molecular interactions minimize charge recombination. These conclusions are supported by measurements of local (nanoscale) conductivity using conductive tip atomic force microscopy. The end-to-side hole coupling in CPB increases hole transfer and low bimolecular charge recombination rates at an interface with C_{70}, resulting in OPVs with a power conversion efficiency of $PCE = 9.6 \pm 0.5$ %, compared with 7.9 ± 0.4 % for an OPV cell based on a non-polar donor, DBP, mixed with C_{70}. Additionally, our calculations of the nearest neighbor electronic couplings are found to provide a reasonable approximation to the range of transfer rates found in the films themselves without having an *a priori* detailed knowledge of the thin film nano- or mesoscopic morphologies. These results suggest paths for rapidly identifying appropriate molecular motifs designed to achieve even higher efficiencies based on the d-a-a' molecular design strategy.

II. Theory

Our purpose is to understand how the donor structure and corresponding solid-state interactions between neighboring molecules affect hole transfer between molecules in a film, and how this process influences the polaron pair dissociation and bimolecular charge recombination at an interface with an acceptor molecule, e.g. C_{70}. Using Marcus theory,[20] the intermolecular hole transfer rate (k_{ht}) has a second-order dependence on the electronic coupling of the initial and final charge transfer states:[21, 22]

$$k_{ht} = {H_{ab}}^2 \left(\frac{\pi}{\hbar\lambda\, k_B T}\right)^{1/2} \exp\left(-\frac{(\Delta G_0+\lambda)^2}{4\lambda\, k_B T}\right), \quad (1)$$

where ΔG_0 is the Gibbs free energy for hole transfer and λ is the reorganization energy of the molecule. Also, $\hbar$ is the reduced Planck's constant, k_B is Boltzmann's constant, and T is the temperature. To increase the hole transfer rate, the intermolecular electronic coupling must be maximized. Calculations of H_{ab} for all possible nearest neighbor orientations in a film can be used to reveal those configurations that contribute the most to the hole transfer process.

Insight into polaron pair and charge recombination dynamics at the donor-C_{70} interface in a solar cell is provided by the analysis of Giebink, et al.[23, 24] The active layer morphology, energy level offsets between D and A, and charge transfer at heterojunctions play important roles in determining the short-circuit current (J_{SC}), open-circuit voltage (V_{OC}), and the fill factor (FF) of OPV cells.[23-27] In steady-state, the J-V characteristics are governed primarily by polaron-pair and free charge recombination dynamics at the D-A junction.[23] Thus:

$$J_{SC} = q\,\frac{\boldsymbol{k_{ppd}}}{k_{ppd}+\boldsymbol{k_{ppr}}} J_x, \quad (2)$$

and

$$qV_{OC} = \Delta E_{DA} - nk_B T \ln\left(qa\,\frac{\boldsymbol{k_{ppr}}}{\boldsymbol{k_{ppd}}+k_{ppr}}\,\frac{\boldsymbol{k_{rec}} H_D N_A}{J_{SC}}\right), \quad (3)$$

where J_x is the exciton flux density at the D-A junction, k_{ppr} is the polaron pair (PP) recombination rate, k_{ppd} is the PP dissociation rate, k_{rec} is the polaron bimolecular recombination rate, and ΔE_{DA} = $LUMO_A$ – $HOMO_D$. Here, $LUMO_A$ is lowest unoccupied molecular orbital of the acceptor, and $HOMO_D$ is highest occupied MO of the donor. Also, n is the ideality factor that is related to the voltage distribution across the interface, which includes the effects of interfacial recombination of an electron in the acceptor with a trap on the donor, a is the width of the polaron-pair formation region, H_D is the trap density of states, and N_A is the density of states in $LUMO_A$. One means for increasing *PCE* is to ensure that k_{ppd} » k_{ppr}, and that bimolecular recombination in the film bulk is minimized, corresponding to $k_{rec} \to 0$.

Under forward bias, the injected electron and hole densities (n_I and p_I, respectively) contribute to the current density, J. Assuming Langevin charge recombination and $n_I = p_I$ at the interface, then:[24]

$$\frac{dn_I}{dt} = \frac{J(t)}{q \cdot a} - k_{rec} \cdot {n_I}^2 + k_{ppd} \cdot \zeta, \tag{4}$$

According to Langevin theory, k_{rec} is proportional to the charge carrier mobility in the blend. The PP density, ζ, is then found using: [24]

$$\frac{d\zeta}{dt} = k_{rec} \cdot {n_I}^2 - k_{ppd} \cdot \zeta - k_{ppr} \cdot \zeta. \tag{5}$$

The rates, k_{rec}, k_{ppr}, and k_{ppd} are obtained from transient measurements of polaron pair state electroluminescence generated at the donor-acceptor interface.

III. EXPERIMENTAL METHODS

Patterned indium tin oxide (ITO)-coated glass substrates (9-15 Ω/sq.; Lumtec) were detergent and solvent cleaned, followed by snow cleaning[28] in air at 100°C, and exposed to ultraviolet light and ozone for 10 min prior to loading into a vacuum thermal evaporation (VTE) chamber (base pressure of $<1 \times 10^{-7}$ torr). Source materials: CPB (Sigma Aldrich, sublimed grade), CTB (Lumtec, sublimed grade), DBP (Lumtec, sublimed grade), C_{60} (MER, sublimed grade), and C_{70} (SES, sublimed grade), were further purified by a single cycle vacuum thermal gradient purification step. MoO_3 (Sigma Aldrich), bathophrenanthroline (BPhen, Lumtec, sublimed grade), and Ag (Alfa Aesar, 99.999% pure) were used as received. The device area is 11 mm^2 as defined by a patterned ITO anode and deposition of the top cathode contact through a shadow mask. The deposition rate for all layers was 1.0 Å/s, except for the DBP:C_{70} layer that was deposited at 0.22 Å/s: and 1.78 Å/s for DBP and C_{70}, respectively. The D-A blends are reported as volume ratios. Film thicknesses and optical constants were measured using variable-angle spectroscopic ellipsometry. Three mixed heterojunction (HJ) solar cells were fabricated with the following structure: glass/indium-tin-oxide/MoO_3 (10 nm)/D:A HJ/BPhen:C_{60} (8 nm)/BPhen (5 nm)/Ag (100 nm), where C_{70} was used as the acceptor. The donors were the non-polar DBP, and the d-a-a' molecules, CTB, and CPB. Also, the exciton blocking and electron conducting layer was 4,7-diphenyl-1, 10-phenanthroline (BPhen) mixed with C_{60} and capped with neat BPhen.

The external quantum efficiencies (*EQEs*) of the OPV cells were measured using a lock-in amplifier and a fiber-coupled monochromated Xe arc-discharge lamp chopped at 200 Hz. The *EQE* experimental error is ±5% due to lamp intensity variations. The optical power was

calibrated using a National Institute of Standards and Technology-traceable Si photodetector. Photovoltaic performance was measured using a semiconductor parameter analyzer and illumination from a simulated air mass 1.5 Global (AM1.5G) filtered source whose intensity was measured with a National Renewable Energy Laboratory-traceable KG-5 filtered Si reference cell. The measured J_{SC} were within 3% of that calculated by integration of the *EQE* from $\lambda = 350$ nm to 900 nm. We primarily used J_{SC} from the integrated *EQE* to determine *PCE*. Experimental errors for V_{OC} and *FF* arise from variations between devices, and the error in J_{SC} (±5%) is primarily due to uncertainties in the intensity of the light source, which also dominates the error in *PCE*.

The electrical conductivity of each D-A blend was calculated from the resistivity of the layer measured from fits[23] to the slope of the forward-biased OPV cell in the series resistance (R_s) dominated high forward bias (1.2 V – 2 V) region versus active layer thickness (l = 40, 60, and 80 nm),[29] using fits to the dark *J-V* curves following the ideal diode formalism of Giebink, et al.[19] (see Eq. 15b, ref. 19). The OPV cells were tested from -1.0 V to 2.0 V bias. Fitting of the dark *J-V* data for CPB:C_{70}, CTB:C_{70}, and DBP:C_{70} solar cells (performance parameters reported in Table I) and corresponding simulations based on these fits are provided in Fig. 1a. Figure 1b shows only the high current region where the functional form is clearly linear, corresponding to Ohmic behavior Furthermore, the *J-V* characteristics of the CTB:C_{70} cell were obtained up to 15 V forward bias. Over that entire voltage range, R_s was constant, indicating a lack of significant charge injection even at that highest currents measured.

Conductive- and photoconductive-tip AFM (C-AFM and PC-AFM respectively) measurements were performed using an Asylum Research MFP-3D stand-alone atomic force

microscope under ultra-pure Ar gas. A Pt-Ir5-coated contact-mode AFM probe (Nanosensors, ATEC-CONTPt, spring constant 0.2 N/m) was simultaneously used for the top contact, topography tracking and current measurement. A voltage of 1.5 V was applied in reference to the ITO anode for dark hole current C-AFM measurements on neat donor films deposited on ITO/MoO_3. A λ = 405 nm wavelength diffraction-limited laser beam attenuated by neutral density filters was focused and aligned to the probe to illuminate the samples at ~10^4 W/m^2. The D-A blends deposited on ITO/MoO_3 and ITO/PEIE (ethoxylated polyethylenimine) for hole and electron PC-AFM measurements, respectively. For each film, 3 - 5 different scan areas were sampled, and the data from each pixel was averaged. The tip contact area of 110 nm^2 was estimated using the Hertzian contact model[30].

The polaron pair luminescence spectra were measured at normal incidence using a fiber-coupled monochromator (Princeton Instruments SP-2300i) equipped with a CCD detector array (PIXIS:400). The relative spectral intensity was calibrated using a tungsten-halogen lamp. The polaron pair luminescence from the donor-C_{70} junction is identified by a broad emission peak in the red-near infrared (NIR) wavelength range. The transient electroluminescence (EL) from the PP states was obtained using a 20 Hz square voltage pulse with a width of 10μs to 20μs. The transient EL turn-on was detected by Si APD (Hamamatsu C5460) with 0.2pW/Hz0.5 noise equivalent power. Pulse currents of 50 mA, 60 mA, 70 mA, and 80 mA were used. Since there was no dependence on drive current, we only show data at 70 mA. Transients were modeled using Eq. (4) and (5) to obtain k_{ppd}, k_{ppr}, and k_{rec}. Fitting errors were calculated from the sum of the modeled transient data at different applied currents, leading to 95% confidence intervals.

The ground state dipoles and reorganization energies of isolated donor molecules were calculated at the DFT level using the B3LYP hybrid functional along with the 6-31G** polarized double-ζ basis set.[31-33] The hole transfer coupling integrals and transfer rates[34, 35] for all nearest neighbor orientations within the donor films were calculated using initial and final charge transfer states from constrained DFT with B3LYP/6-31G** as implemented in the Schrödinger Material Science Suite, version 2014-3, with Jaguar version 8.5 release 13. The coupling calculations directly evaluate the off-diagonal coupling matrix elements of the Hamiltonian between these wave functions. This approach evaluates the total coupling from all states between donor (neutral)-acceptor (cation), not only contributions from frontier orbital levels[36].

The nearest neighbor distances and orientations for the molecules in each donor film were taken from the corresponding published crystal structures that are accurate to within 4 Å.[13, 36] Convergence of the coupling integrals was confirmed by carrying out calculations using larger augmented basis sets (6-31++G**). Adding diffuse functions did not lead to notable changes in the hole coupling parameters.

IV. RESULTS

Three mixed heterojunction solar cells were studied based on the donors in Scheme 1 and Fig. 2a: two dipolar complexes with a d-a-a' structure: CPB (with dipole moment of 12.0 D) and CTB (14.5D), and an archetype non-polar molecule, DBP (0 D) for comparison. The direction and relative magnitudes of the dipole moments are indicated by arrows in the figure. Notably, the absorption spectra of CPB and CTB extend into the NIR, with the response of CTB reaching λ = 850 nm (Fig. 2b).[13, 18]

The *J-V* characteristics under 1 sun, AM1.5G illumination and the *EQE* vs.wavelength of CPB:C_{70} (1:1 by vol., 80 nm), CTB:C_{70} (1:1, 80 nm), and DBP:C_{70} (1:8, 60 nm) OPV mixed cells are shown in Fig. 3 and Table I. Both the CPB:C_{70} and CTB:C_{70} cells have significantly higher J_{SC} *vs*. the DBP:C_{70} cell due to their broader absorption spectra. The V_{OC} scales with the difference in HOMO levels of the donors, thereby leading to differences in ΔE_{DA} according to Eq. (3).

In Fig. 4 we show the dependence of OPV performance on mixed layer thickness (l). Although the peak absorbance of CPB is significantly less than that of either DBP or CTB, the CPB:C_{70} cell has the highest $PCE = 9.6 \pm 0.5$ %. Both V_{OC} and FF of the CPB and CTB-based cells are independent of active layer thicknesses, $l \leq 80$ nm, whereas J_{SC} increases in the range from $l = 40$ to 80 nm. For the DBP:C_{70} cell, V_{OC} decreases and J_{SC} remains constant for $l > 60$ nm. The trends in J_{SC} follow the conductivities of the corresponding active layers (see Table II), with the CTB:C_{70} blend having the highest photocurrent as well as the highest conductivity. The performances of the CPB and CTB based cells are significantly higher than previously published using these dipolar donors.[13] This difference is attributed to the higher purity of CTB and CPB source materials resulting additional purification by train sublimation, and the use of the BPhen:C_{60} cathode buffer layer that improves the electron collection at the active layer/cathode interface[11].

The dark hole currents of CPB and CTB were mapped by C-AFM at +1.5 V, with results in Fig. 5. The average dark hole current density of CTB is 130 ± 30 nA/μm^2, which is four times that of CPB (30 ± 10 nA/μm^2). This quantitatively agrees with the four-fold increase in conductivity of the corresponding mixed D-A layers, and in hole transfer rates of the neat donors

(see Table II), from which we conclude that differences in the *J-V* characteristics of the donor-C_{70} blended OPVs are due to differences in hole transfer between neighboring donor molecules in the films.

The emission spectra of the PP states at the CPB-C_{70} interface (peak PP emission wavelength, λ_{PP} = 938 nm), CTB-C_{70} interface (λ_{PP} = 981 nm), and DBP-C_{70} junctions (λ_{PP} = 886 nm) are shown in Fig. 6a. Transient electroluminescence (EL) at the wavelength of peak PP emission is shown in Fig. 6b. The turn-on transients were modeled using Eqs. (4) and (5), as shown by solid lines in Fig. 6b. The PP dissociation and recombination rates along with the charge recombination coefficients of CPB:C_{70}, CTB:C_{70} vs. DBP:C_{70} devices obtained from these data are provided in Table III.

V. DISCUSSION

The inhomogeneities apparent in the photocurrent maps for CPB:C_{70} *vs*. DBP:C_{70} mixtures suggest that percolating paths exist that lead to conduction of both holes and electrons to their respective electrodes in OPV cells (Figs. 7a and 7b, respectively). The hole photocurrent density in CPB:C_{70} is significantly higher than for DBP:C_{70} (300 ± 20 vs. 23 ± 5 nA/μm^2 respectively), while the electron photocurrent density for CPB:C_{70} is twice that of DBP:C_{70}. Since C_{70} is common to both mixtures, we can conclude that the differences in hole transfer along percolating pathways established by the donor molecules are responsible for the differences in the conductivity of the respective D-A blends.

Intermolecular electronic coupling in the donor films was theoretically evaluated using direct evaluation of the coupling parameter between constrained DFT initial and final states. The

constrained DFT approach[19] minimizes errors that occur due to neglect of polarization in the energy splitting in the dimer method[37] by assigning charge to a single molecule within the pair when calculating the wavefunction. Moreover, Bredas, *et. al.*, have shown that the principal error introduced by considering the dimer only, rather than the complete crystals, is in the difference in site energies while the transfer integral is nearly the same for the dimer and a larger system that takes even more molecules into consideration.[37]

The CPB and CTB moieties have electron density localized in the HOMO on the ditolylamino phenyl (in CPB)/thienyl (in CTB) group (relative d-group). The LUMO is delocalized across the benzothiadiazole and dicyanovinylene units (a and a'-groups), as shown by the orbital contours in Fig. 2a. The d-a-a' structure results in large ground state dipoles directed along the molecular backbones (c.f. Table II). In both compounds, molecules are cofacially stacked in an antiparallel manner along their long molecular axes. The stacks are further arranged in a herringbone pattern with each stack tilted at an oblique angle with respect to a neighboring stack. The packing motif enables the ditolylamino end group of one molecule to nest against the side of a pair of molecules in an adjacent stack. For comparison to the d-a-a' donors, we have also carried out theoretical studies of DBP, another high performance OPV donor material.[38-40] For DBP, the HOMO and LUMO electron densities are delocalized over the perylene core, leading to a zero ground state dipole moment. The molecules are arranged in a series of collinear slip-stacks with the pendant phenyl rings separating side-to-side neighboring stacks.

The hole coupling and transfer rates between CPB, CTB, and DBP molecules were theoretically estimated as described in the Experimental Methods section, and are given in Table

II. Our initial approach was to base our calculations on each donor dimer in the gas phase, with the dimer coordinates taken from the reported crystal structures. We carried out several additional calculations to investigate whether environmental effects from neighboring molecules are important in estimating coupling and carrier transport rates for the three donors studied here. We investigated these medium effects using a continuum dielectric approach, along with embedding the molecules in point charges, representative of the polarization and electrostatic interactions in the condensed phase. The effective dielectric constants for CPB, CTB, and DBP were calculated using their computed polarizability and the Clausius-Mossotti relation[42] at the B3LYP/6-31G** level of theory. These dielectric constants were then used in a continuum solvation model to calculate the reorganization. As shown in Table II, values of λ_{hole} are not significantly different between those obtained for the gas phase and those including the effective medium dielectric properties. Electrostatic interactions were found to have a minor effect on λ_{hole}. For CTB, replacing one molecule of the dimer by electrostatic charges gives a reorganization energy of 0.133 eV, very close to the gas phase and solvent based values of 0.133 and 0.130 eV, respectively (Table II).

Medium effects may influence the coupling integrals as well. This was investigated using electrostatic charge embedding. For example, the cofacial CTB dimer (Fig. 8f) can be considered embedded between two other parallel molecules as reported in crystal structure data. First the electrostatic potential (ESP) charges were calculated for four cofacially stacked molecules. This ensemble was represented by the CTB dimer (Fig. 8f) and one CTB molecule above and one below the dimer. The molecules above and below the dimer were substituted with the ESP point charges and the intra-dimer coupling integrals were calculated. This resulted in intra-dimer

coupling values for holes and electrons of 0.125 and 0.062 eV, compared to 0.120 and 0.068 eV, respectively for the dimer in the gas phase. Thus, for these donor systems, environmental effects play only a minor role in intermolecular electronic coupling.

The calculated trends between CPB, CTB, and DBP are consistent with the conductivity in the corresponding donor-C_{70} layers (see Table II). Based on the largest hole transfer coupling (expected to yield the highest transfer rates), holes are most efficiently conducted via an end-to-side (Fig. 8a) orientation in CPB. Lower values of H_{ab} and k_{ht} calculated for cofacial π-stacking (Fig. 8b, d) are comparable to that of a weaker end-to-side coupling between molecules (Fig. 8c). In contrast for CTB, stronger coupling is found for end-to-side packing (Fig. 8e) although a cofacial orientation (Fig. 8f) gives the highest rate for k_{ht}.

High hole transfer coupling energies and rates in CTB are also found for other lateral (Fig. 8g) and cofacial (Fig. 8h) orientations between adjacent molecules. As expected for the planar, non-polar DBP, the hole transfer coupling and rate are significantly higher for the cofacial orientation in DBP (Fig. 8i) than values found in side-to-side orientations (Fig. 8j and 8k). Therefore, the dominant pathway for hole transfer in DBP is likely in the cofacial stacking direction. In summary, for CPB, only end-to-side orientations lead to efficient hole transfer, whereas in CTB both cofacial and end-to-side interactions contribute to the hole transfer and high conductivity, while the most probable direction for hole transfer in DBP is only along the cofacial π–π stacks. The trends in coupling lead to higher hole transfer rates in d-a-a' molecules, with the highest k_{ht} for CTB (see Table II).

The transient EL measurements indicate that the charge recombination rate is the highest for the DBP:C_{70} blend, followed by a smaller k_{rec} for CTB:C_{70}, and with the lowest k_{rec} for CPB:C_{70}

(see Table III). Polaron pair dissociation dominates recombination for all three devices (i.e. k_{ppd} » k_{ppr}) leading to a dissociation efficiency of $\eta_{ppd} = k_{ppd}/(k_{ppd} + k_{ppr}) \approx 1$, as expected for the blended D-A heterojunctions in all three cells. However, the CPB:C_{70} OPV cell has the highest k_{ppd} and lowest k_{ppr}. We conclude, therefore, that the observed photocurrent trend of CTB > CPB > DBP – based solar cells is primarily due to the differences in absorption in the active layers, while the corresponding high power conversion efficiency for CPB:C_{70} is mainly due to slow bimolecular charge recombination that affects the fill factor. We also note that Chang, *et al*. have shown that morphological effects in blends containing the donor CTB (and by inference, CPB) can also play a significant role in charge separation,[43] which also effects the ratio of k_{ppr} to k_{ppd} and hence, *FF*[44].

Interestingly, the conductivities of the three molecular species also follow a similar progression in hole hopping rates (k_{ht}, see Table II) between nearest neighbors. Hence, we can infer the *macroscopic* conductive properties from the *nanoscopic* nearest neighbor interactions in these blends. While we have been unable to find direct evidence for crystallization in the blends using x-ray and other microscopic probes, the C-AFM and PC-AFM maps clearly show regions of high and low conductivities, from which we infer the presence of extended percolating conductive pathways for both holes and electrons. The computational efficiency resulting from considering only nearest neighbor interactions should prove helpful in rapidly identifying appropriate donor and acceptor molecules for use in future, high efficiency OPV cells employing D-A blended active regions.

V. CONCLUSIONS

Our findings provide insight into the role played by high molecular ground state dipole moments in donor-acceptor-acceptor' materials in controlling the solid-state molecular orientations that promote hole transfer in D-A mixed HJs. We find that the high dipole moment d-a-a' materials studied here effectively dimerize in the solid state, leading to net cancelation of their high dipole moments in the solid state. These chromophore dimers then pack in a herringbone arrangement, which leads to high conductivity and photocurrent generation in organic solar cells using these materials as donors with a C_{70} acceptor. We find that dipole-induced end-to-side orientations in d-a-a' molecules can lead to improved hole transport, and hence to significantly reduced charge recombination, ultimately resulting in solar cells with high V_{OC}, *FF* and *PCE*. The highest photocurrent (J_{SC} = 16.7 ± 0.8 mA/cm^2) is generated in OPV cells based on CTB, which has the largest single molecule dipole moment of 14.5 D, and gives the largest intermolecular orbital overlap and hole transfer rate. However, the most efficient polaron pair dissociation and the lowest charge recombination was achieved for CPB-based solar cell, leading to higher *FF*, V_{OC}, and *PCE* = 9.6 ± 0.5 %. This work shows that electron couplings and charge transfer rates between nearest neighbors can be predictive indicators of the macroscopic conductive properties in films. Indeed, d-a-a' donors with deeper lying HOMO energy levels, higher peak absorption and broader absorption ranges than CPB and CTB molecules have recently been reported.[18] In addition, we have shown that the spatial extent and strength of *intra*molecular charge transfer within a donor molecule can strongly influence *inter*molecular charge hopping in donor films, thereby leading to significant improvements in the efficiency of organic solar cells.

AUTHOR INFORMATION

Corresponding Author

*Stephen Forrest, stevefor@umich.edu

Acknowledgements

We thank Drs. Mathew D. Halls and Alexander Goldberg of Schrödinger, Inc. for help with the quantum mechanical studies and Schrödinger Inc. for providing access to their Materials Science Suite of software used for the molecular modeling and electron transfer studies. We thank Byeongseop Song for fabrication and testing of DBP:C_{70} cells and Xiaozhou Che for fabrication and testing of CTB:C_{70} cells. Funding was provided in part by the Center for Solar and Thermal Energy Conversion at the University of Michigan, an Energy Frontier Research Center funded by the Department of Energy through the Office of Science, Office of Basic Energy Sciences under Award number DE-SC0000957 (O.L.G. – experiments and analysis; J.A.A., P.G. – C-AFM measurements), the Air Force Office of Scientific Research (X.L. – transient EL measurements and fitting; S.R.F. -- analysis) and NanoFlex Power Corporation (M.E.T. – analysis; P.D. – DFT/CDFT calculations).

REFERENCES

1. G. Yu, J. Gao, J. C. Hummelen, F. Wudl and A. J. Heeger, Science **270** (5243), 1789-1791 (1995).

2. J. J. M. Halls, C. A. Walsh, N. C. Greenham, E. A. Marseglia, R. H. Friend, S. C. Moratti and A. B. Holmes, Nature **376** (6540), 498-500 (1995).

3. P. Peumans, S. Uchida and S. R. Forrest, Nature **425** (6954), 158-162 (2003).

4. M. Y. Chan, C. S. Lee, S. L. Lai, M. K. Fung, F. L. Wong, H. Y. Sun, K. M. Lau and S. T. Lee, Journal of Applied Physics **100** (9), 094506 (2006).

5. A. W. Hains and T. J. Marks, Applied Physics Letters **92** (2), 023504 (2008).

6. R. Steim, F. R. Kogler and C. J. Brabec, Journal of Materials Chemistry **20** (13), 2499-2512 (2010).

7. M. Hirade and C. Adachi, Applied Physics Letters **99** (15), 153302 (2011).

8. B. E. Lassiter, G. Wei, S. Wang, J. D. Zimmerman, V. V. Diev, M. E. Thompson and S. R. Forrest, Applied Physics Letters **98** (24), 243307-243303 (2011).

9. A. N. Bartynski, C. Trinh, A. Panda, K. Bergemann, B. Lassiter, J. D. Zimmerman, S. R. Forrest and M. E. Thompson, Nano Letters **13**, 3315-3320 (2013).

10. O. L. Griffith and S. R. Forrest, Nano Letters **14** (5), 2353-2358 (2014).

11. C. W. Schlenker, V. S. Barlier, S. W. Chin, M. T. Whited, R. E. McAnally, S. R. Forrest and M. E. Thompson, Chemistry of Materials **23** (18), 4132-4140 (2011).

12. K. Cnops, B. P. Rand, D. Cheyns, B. Verreet, M. A. Empl and P. Heremans, Nature Communications **5**, 4406 (2014).

13. Y. H. Chen, L. Y. Lin, C. W. Lu, F. Lin, Z. Y. Huang, H. W. Lin, P. H. Wang, Y. H. Liu, K. T. Wong, J. Wen, D. J. Miller and S. B. Darling, Journal of the American Chemical Society **134** (33), 13616-13623 (2012).

14. A. Dieckmann, H. Ba□ssler and P. M. Borsenberger, The Journal of Chemical Physics **99** (10), 8136 (1993).

15. M. Van der Auweraer, F. C. De Schryver, P. M. Borsenberger and H. Bässler, Advanced Materials **6** (3), 199-213 (1994).

16. H. Burckstummer, E. V. Tulyakova, M. Deppisch, M. R. Lenze, N. M. Kronenberg, M. Gsanger, M. Stolte, K. Meerholz and F. Wurthner, Angewandte Chemie-International Edition **50** (49), 11628-11632 (2011).

17. F. Wurthner and K. Meerholz, Chemistry **16** (31), 9366-9373 (2010).

18. H.-C. Ting, Y.-H. Chen, L.-Y. Lin, S.-H. Chou, Y.-H. Liu, H.-W. Lin and K.-T. Wong, ChemSusChem **7** (2), 457-465 (2014).

19. B. Kaduk, T. Kowalczyk and T. Van Voorhis, Chemical Reviews **112** (1), 321-370 (2012).

20. R. A. Marcus, The Journal of Chemical Physics **24** (5), 966 (1956).

21. W.-Q. Deng and W. A. Goddard III, Journal of Physical Chemistry B **108**, 8614-8621 (2004).

22. B. Baumeier, J. Kirkpatrick and D. Andrienko, Physical Chemistry Chemical Physics **12** (36), 11103-11113 (2010).

23. N. C. Giebink, G. P. Wiederrecht, M. R. Wasielewski and S. R. Forrest, Physical Review B **82** (15), 155305 (2010).

24. N. C. Giebink, B. E. Lassiter, G. P. Wiederrecht, M. R. Wasielewski and S. R. Forrest, Physical Review B **82** (15), 155306 (2010).

25. M. D. Perez, C. Borek, S. R. Forrest and M. E. Thompson, J Am Chem Soc **131** (26), 9281-9286 (2009).

26. R. A. Marsh, C. R. McNeill, A. Abrusci, A. R. Campbell and R. H. Friend, Nano Letters **8** (5), 1393-1398 (2008).

27. W. J. Potscavage, S. Yoo and B. Kippelen, Applied Physics Letters **93** (19), 193308 (2008).

28. N. Wang, J. D. Zimmerman, X. Tong, X. Xiao, J. Yu and S. R. Forrest, Applied Physics Letters **101** (13), 133901 (2012).

29. S. Choi, W. J. Potscavage and B. Kippelen, Journal of Applied Physics **106** (5), 054507 (2009).

30. K. Daeinabi and M. H. Korayem, Micro & Nano Letters **6** (9), 794 (2011).

31. A. D. Becke, The Journal of Chemical Physics **98** (7), 5648-5652 (1993).

32. C. Lee, W. Yang and R. G. Parr, Physical Review B **37** (2), 785-789 (1988).

33. R. Krishnan, J. S. Binkley, R. Seeger and J. A. Pople, The Journal of Chemical Physics **72** (1), 650-654 (1980).

34. Q. Wu and T. Van Voorhis, The Journal of chemical physics **125** (16), 164105 (2006).

35. Q. Wu and T. Van Voorhis, Journal of Chemical Theory and Computation **2**, 765-774 (2006).

36. J. D. Debad, J. C. Morris, V. Lynch, P. Magnus and A. J. Bard, Journal of the American Chemical Society **118** (10), 2374-2379 (1996).

37. E. F. Valeev, V. Coropceanu, D. A. da Silva, S. Salman and J. L. Bredas, Journal of the American Chemical Society **128** (30), 9882-9886 (2006).

38. Y.-q. Zheng, W. J. Potscavage, T. Komino, M. Hirade, J. Adachi and C. Adachi, Applied Physics Letters **102** (14), 143304 (2013).

39. X. Xiao, J. D. Zimmerman, B. E. Lassiter, K. J. Bergemann and S. R. Forrest, Applied Physics Letters **102** (7), 073302 (2013).

40. Z. Wang, D. Yokoyama, X.-F. Wang, Z. Hong, Y. Yang and J. Kido, Energy Environ. Sci. **6** (1), 249-255 (2013).

TABLE I. Electrical parameters of CPB:C_{70}, CTB:C_{70}, and DBP:C_{70} solar cells.

D:A	HOMO of D,[a] eV	V_{OC}, V	J_{SC},[b] mA/cm^2	*FF*, %	*PCE*, %
CPB:C_{70} 80 nm	5.4 ±0.1	0.92 ±0.01	15.8 ± 0.7	67 ± 1	9.6 ± 0.5
CTB:C_{70} 80 nm	5.3 ±0.1	0.80 ±0.01	16.7 ± 0.8	60 ± 1	8.0 ± 0.4
DBP:C_{70} 60 nm	5.4 ±0.1	0.92 ±0.01	13.6 ± 0.7	63 ± 1	7.9 ± 0.4

[a] HOMO levels relative to vacuum of neat donor films as measured by UV photoelectron spectroscopy were taken from refs. [7, 13]

[b] J_{SC} obtained from *EQE* spectra. Values are within 3% of *J-V* data obtained using 1 sun AM 1.5G simulated illumination.

TABLE II. Properties of donor-acceptor (D:A) blends.

D:A	Dipole moment [a]	$\sigma_{D:A}$ [b]	ε [c]	λ_{hole}, eV [d]		k_{ht} [e]
	D	x10^{-5}S/cm		gas phase	ε continuum	x10^{12} s^{-1}
CPB:C_{70}	12.0	1.4 ± 0.4	4.728	0.110	0.142	2.8
CTB:C_{70}	14.5	5.2 ± 0.1	4.748	0.133	0.130	200
DBP:C_{70}	0.0	0.4 ± 0.1	5.033	0.104	0.105	2.5

[a] Calculated molecular dipole moments of donors using DFT (B3LYP/6-31G**) of the donors used in the blends.

[b] Conductivities of D-A blends.

[c] Calculated dielectric constant estimated as described in the text.

[d] Reorganization energy for holes, based on a gas phase model and a dielectric continuum (solvent) based model.

[e] Hole transfer rate between two nearest donors in the direction of the strongest hole transfer coupling.

TABLE III. Rate constants of various donor-acceptor blends.

D:A	k_{rec},[a] $x10^{-6}$ cm^3/s	k_{ppd},[b] $x10^{10}$ s^{-1}	k_{ppr},[c] $x10^{6}$ s^{-1}
CPB:C_{70}	1.29 ± 0.02	55.3 ± 0.4	1.2 ± 0.1
CTB:C_{70}	9.7 ± 1.4	0.3 ± 0.1	4.6 ± 0.1
DBP:C_{70}	39.6 ± 3.9	0.8 ± 0.1	3.9 ± 0.2

[a] Bimolecular charge (or polaron) recombination rate

[b] Polaron pair dissociation rate

[c] Polaron pair recombination rate

FIGURE CAPTIONS

Fig. 1: (a) Measured dark (line) and simulated current density vs. voltage (*J-V*) characteristics (red circles) for CPB:C_{70}, CTB:C_{70}, and DBP:C_{70} solar cells. (b) Corresponding dark *J-V* data for voltage >1.2 V, also showing a linear fit in this voltage range.

Fig. 2: (a) Electron density distributions of the highest occupied molecular orbitals (HOMOs, solid transparent surfaces) and lowest unoccupied MOs (mesh surfaces) of the isolated donor molecules (CPB, CTB, DBP). Both CPB and CTB molecules have a donor-acceptor-acceptor' structure resulting in large ground state dipoles (arrows) in the molecular plane caused by the presence of spatially separated positive (donor, δ^+) and negative (acceptor, δ^-) charge distributions. DBP lacks a dipole moment (indicated by the dot in the center of the molecule). (b) Extinction coefficients of CPB, CTB, and DBP thin films.

Fig. 3: Current density-voltage (*J-V*, top) and external quantum efficiency (*EQE*, bottom) characteristics of CPB:C_{70} (red circles), CTB:C_{70} (blue squares), and DBP:C_{70} (black triangles) solar cells. The *J-V* characteristics are obtained at 1 sun, AM1.5G simulated solar illumination.

Fig. 4: (a) Fill factor, *FF*, (b) open circuit voltage, V_{oc}, and (c) short circuit current, J_{sc} vs. mixed heterojunctions layer thickness, *l*, for CPB:C_{70} (red circles), CTB:C_{70} (blue squares), and DBP:C_{70} (black triangles) cells.

Fig. 5: Conductive-tip atomic force microscope (C-AFM) images of neat 40 nm CTB (top) and CPB (bottom) films on MoO_3 at +1.5V bias. Topography maps are on the right and

corresponding dark hole current maps are on the left for 1 μm x 2 μm image fields, with average dark hole current densities indicated.

Fig. 6: (a) Polaron pair (PP) emission spectra of CPB:C_{70} (red line with circles), CTB:C_{70} (line with squares), and DBP:C_{70} (black line with triangles) solar cells. (b) Transient electroluminescence from the PP state at D-A junctions of CPB:C_{70} (data, circles, solid line, simulation), CTB:C_{70} (squares, data, simulation, dashed line), and DBP:C_{70} (data, triangles, dash-siulation, dotted line) mixtures.

Fig. 7: Photoconductive-tip AFM images of 80 nm thick CPB:C_{70} and DBP:C_{70} films photoexcited at a wavelength of λ = 405 nm (left, topography; right, photocurrent): (a) Hole photocurrent from films deposited on MoO_3. (b) Electron photocurrent measurements for films on ethoxylated polyethylenimine (PEIE). The average photocurrent densities are shown in the bottom left corner of corresponding photocurrent images, each of which is for a 1 μm x 2 μm image field.

Fig. 8: Cofacial and end-to-side nearest neighbor molecular orientations along with corresponding hole transfer coupling energies (H_{ab}, meV) and hole hopping rates (k_{ht}, 10^{12} s^{-1}, in parentheses) calculated for neighboring (a-d) CPB, (e-h) CTB and (i-k) DBP configurations.

Scheme 1

CPB

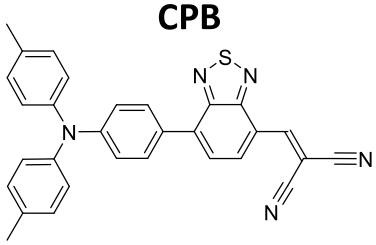

CTB

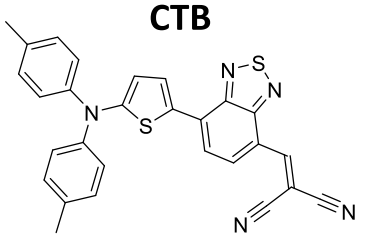

DBP

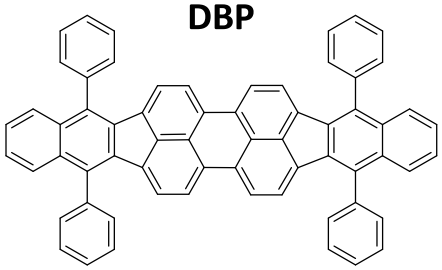

Figure 1 BC13152 15JUL2015

Figure 1

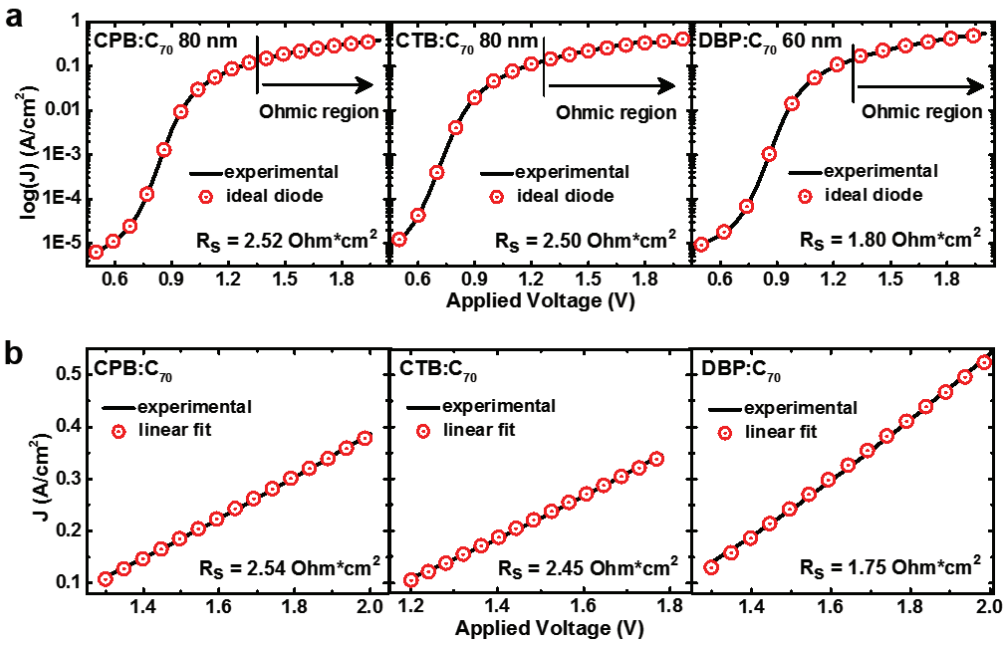

Figure 2 BC13152 15JUL2015

Figure 2

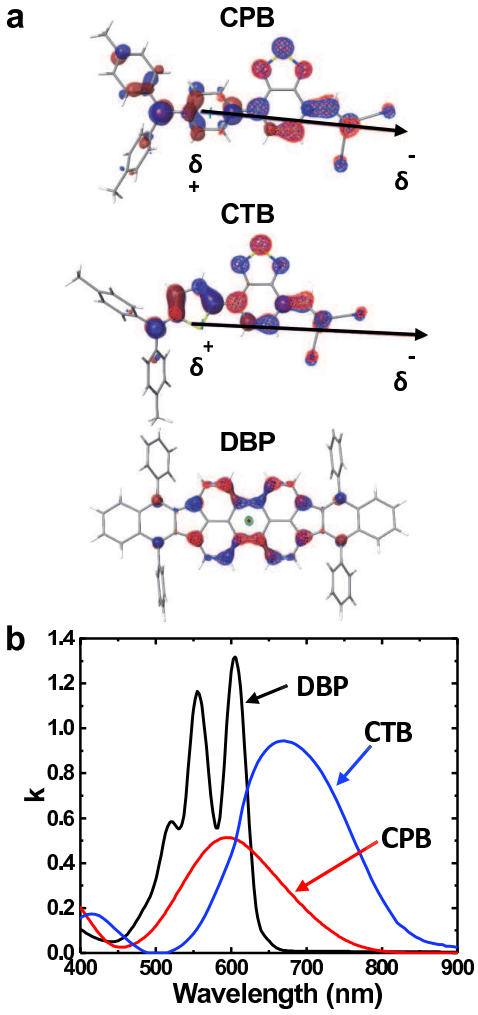

Figure 3 BC13152 15JUL2015

Figure 3

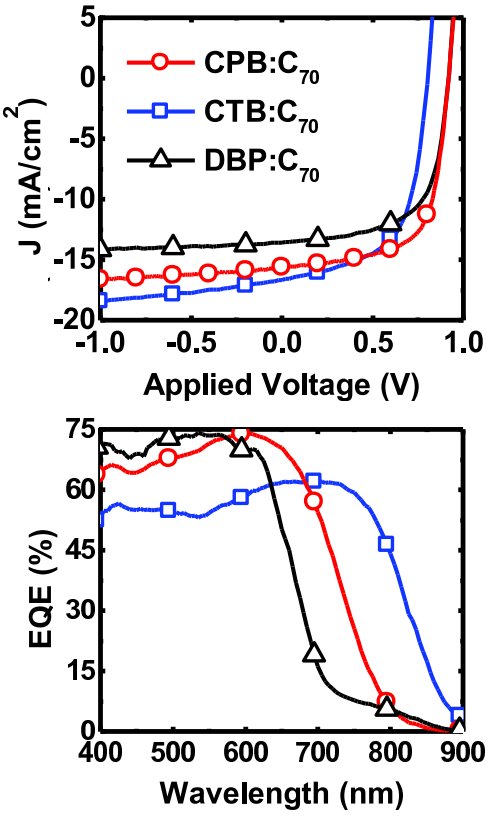

Figure 4 BC13152 15JUL2015

Figure 4

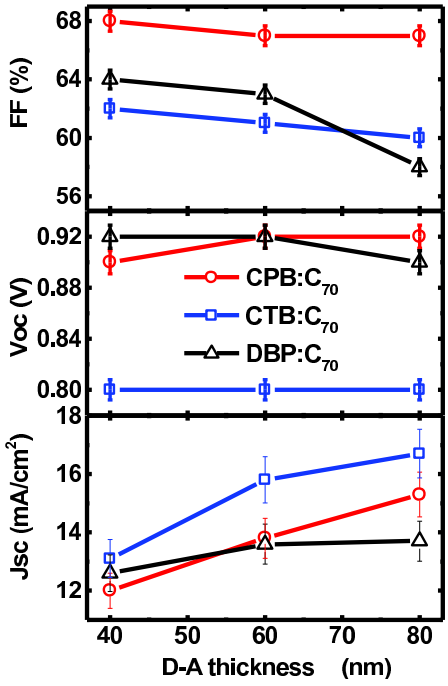

Figure 5 BC13152 15JUL2015

Figure 5

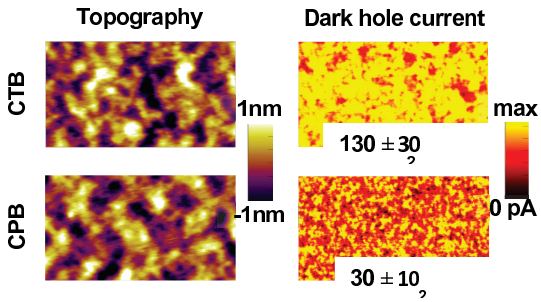

Figure 6 BC13152 15JUL2015

Figure 6

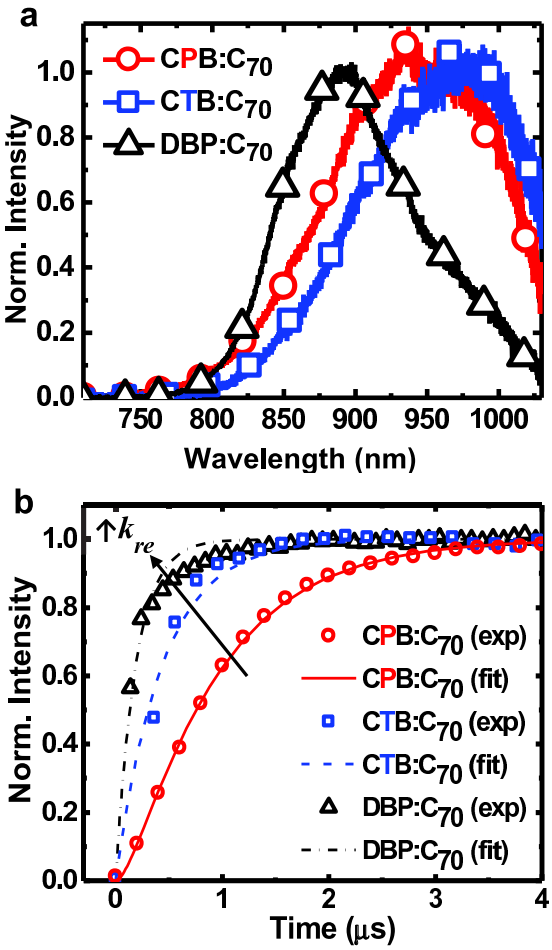
a
CPB:C70
CTB:C70
DBP:C70
Norm. Intensity
1.0
0.8
0.6
0.4
0.2
0.0
750
800
850
900
950
1000
Wavelength (nm)
b
↑kre
CPB:C70 (exp)
CPB:C70 (fit)
CTB:C70 (exp)
CTB:C70 (fit)
DBP:C70 (exp)
DBP:C70 (fit)
Norm. Intensity
0
1
2
3
4
Time (μs)

Figure 7

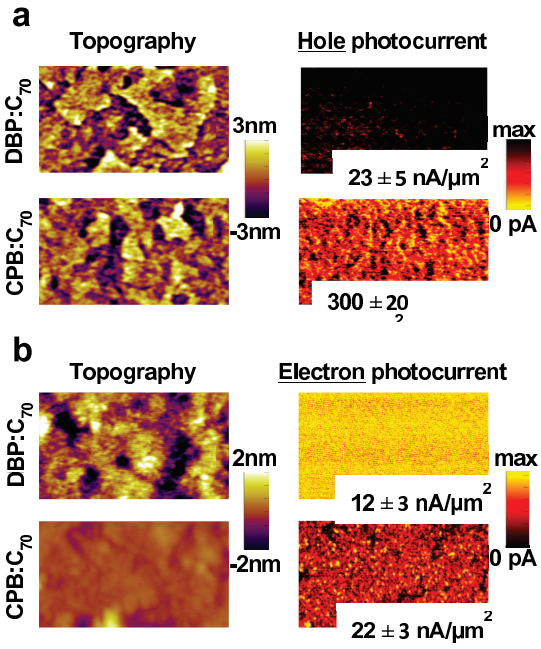

Figure 8 BC13152 15JUL2015

Figure 8

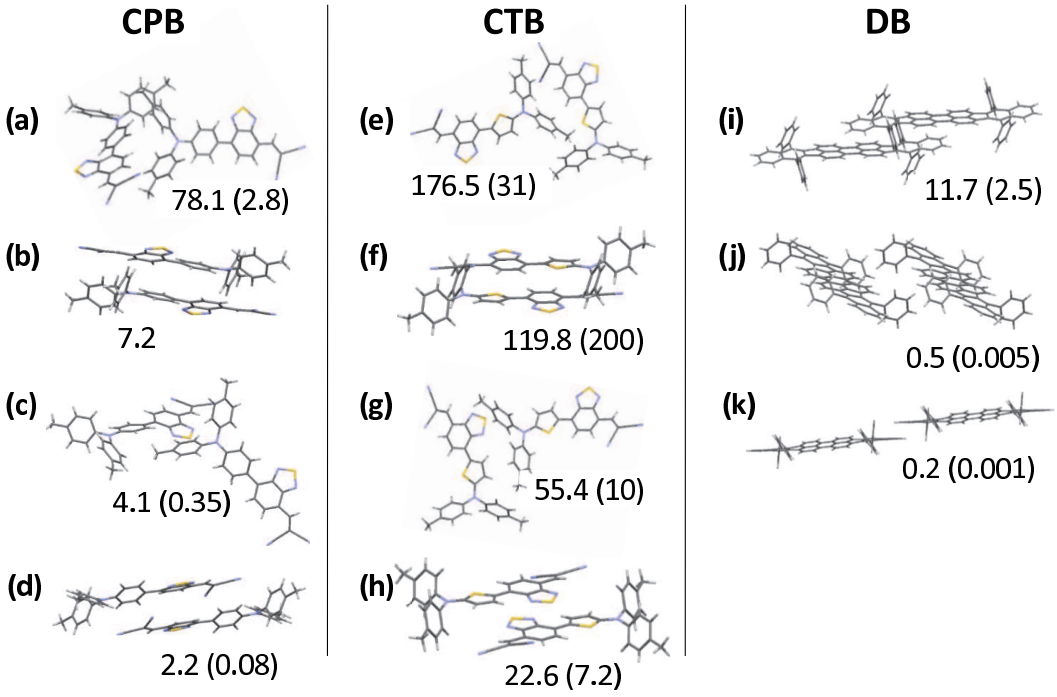

Figure 9 BC13152 15JUL2015